



1 **A Statistical Comparison of Cirrus Particle Size Distributions**
2 **Measured Using the 2D Stereo Probe During the TC⁴,**
3 **SPartICus, and MACPEX Flight Campaigns with Historical**
4 **Cirrus Datasets**

5
6 M. Christian Schwartz^{1,2}

7 Computation Institute, University of Chicago, 5735 South Ellis Avenue, Chicago, IL, 60637, United States
8 Argonne National Laboratory, 9700 Cass Avenue, Bldg. 240, 6.A.15, Lemont, IL, 60439, United States

9
10 *Correspondence to:* M. Christian Schwartz (mcs45@byu.net)



11 **Abstract.** This paper addresses two straightforward questions. First, how similar are the statistics of cirrus particle
12 size distribution (PSD) datasets collected using the 2D Stereo (2D-S) probe to cirrus PSD datasets collected using
13 older Particle Measuring Systems (PMS) 2D Cloud (2DC) and 2D Precipitation (2DP) probes? Second, how similar
14 are the datasets when shatter-correcting post-processing is applied to the 2DC datasets? To answer these questions,
15 a database of measured and parameterized cirrus PSDs, constructed from measurements taken during the Small
16 Particles in Cirrus (SPaRtICus), Mid-latitude Airborne Cirrus Properties Experiment (MACPEX), and Tropical
17 Composition, Cloud, and Climate Coupling (TC⁴) flight campaigns is used.

18 Bulk cloud quantities are computed from the 2D-S database in three ways: first, directly from the 2D-S
19 data; second, by applying the 2D-S data to ice PSD parameterizations developed using sets of cirrus measurements
20 collected using the older PMS probes; and third, by applying the 2D-S data to a similar parameterization developed
21 using the 2D-S data itself. Thereby a parameterized version of what the 2DC would have seen had it flown on the
22 above missions next to the 2D-S is compared to a similarly parameterized version of the 2D-S. It is seen, given the
23 same cloud field and given the same assumptions concerning ice crystal cross-sectional area, density, and radar
24 cross section, that the parameterized 2D-S and the parameterized 2DC predict similar distributions of inferred
25 shortwave extinction coefficient, ice water content, and 94 GHz radar reflectivity. However, the parameterization of
26 the 2DC based on uncorrected data predicts a statistically significant higher number of total ice crystals and a larger
27 ratio of small ice crystals to large ice crystals than does the parameterized 2D-S. The 2DC parameterization based
28 on shatter-corrected data also predicts statistically different numbers of ice crystals than does the parameterized 2D-
29 S, but the comparison between the two is nevertheless more favorable. It is concluded that the older data sets
30 continue to be useful for scientific purposes, with certain caveats, and that continuing field investigations of cirrus
31 with more modern probes is desirable.



32 1 Introduction

33 For decades, in situ ice cloud particle measurements often indicated ubiquitous, high concentrations of the
34 smallest ice particles (Korolev et al., 2013a; Korolev and Field, 2015). If the smallest ice particles are indeed
35 always present in such large numbers, then their effects on cloud microphysical and radiative properties are
36 pronounced. Heymsfield et al. (2002) reported small particles' dominating total particle concentrations (N_{TS}) at all
37 times during multiple Tropical Rainfall Measuring Mission (TRMM) field campaigns, while Field (2000) noted the
38 same phenomenon in mid-latitude cirrus. Lawson et al. (2006) reported N_{TS} in mid-latitude cirrus ranging from ~
39 $.2\text{-}1\text{ cm}^{-3}$ and showed that particles smaller than 50 microns were responsible for 99% of N_T , 69% of shortwave
40 extinction, and 40% of ice water content (IWC). From several representative cirrus cases, Gayet et al. (2002)
41 reported average N_{TS} as high as 10 cm^{-3} and estimated that particles having maximum dimensions smaller than 15.8
42 microns resulted in about 38% of measured shortwave extinction; and Gayet et al. (2004) and Gayet et al. (2006)
43 estimated from a broader set of measurements that particles smaller than 20 microns accounted for about 35% of
44 observed shortwave extinction.

45 However, shattering of ice particles on probe tips and inlets and on aircraft wings has rendered many
46 historical cirrus datasets suspect (Vidaurre and Hallet, 2009; Korolev et al., 2011) due to such shattering's
47 artificially inflating measurements of small ice particle concentrations (see, e.g., McFarquhar et al., 2007; Jensen et
48 al., 2009; and Zhao et al., 2011). Measured ice particle size distributions (PSDs) are used to formulate
49 parameterizations of cloud processes in climate and weather models, so the question of the impact of crystal
50 shattering on the historical record of ice PSD measurements is one of significance (Korolev and Field, 2015).

51 Post-processing of optical probe data based on measured particle inter-arrival times (Cooper, 1978; Field et
52 al., 2003; Field et al., 2006; Lawson, 2011; Jackson et al., 2014; Korolev and Field, 2015) has become a tool for
53 ameliorating contamination from shattered artifacts. Shattered particle removal is based on modeling particle inter-
54 arrival times by a Poisson process, assuming that each inter-arrival time is independent of all other inter-arrival
55 times. Jackson and McFarquhar (2014) posit that particle clustering (Hobbs and Rangno, 1985; Kostinski and Shaw,
56 2001; Pinsky and Khain, 2003; Khain et al., 2007), which would violate this basic assumption, is not likely a matter
57 of significant concern as cirrus particles are naturally spread further apart than liquid droplets and sediment over a
58 continuum of size-dependent speeds.

59 A posteriori shattered particle removal should be augmented with design measures such as specialized



60 probe arms and tips (Vidaurre and Hallet, 2009; Korolov et al., 2011; Korolev et al., 2013a; Korolev and Field,
61 2015). Probes must also be placed away from leading wing edges (Vidaurre and Hallet, 2009; Jensen et al., 2009),
62 as many small particles generated by shattering on aircraft parts are likely not be filtered out by shatter-recognition
63 algorithms.

64 The ideal way to study the impact of both shattered particle removal and improved probe design is to fly
65 two versions of a probe—one with modified design and one without—side by side and then to compare results from
66 both versions of the probe both with and without shattered particle removal. Results from several flight legs made
67 during three field campaigns where this was done are described in three recent papers: Korolev et al. (2013b),
68 Jackson and McFarquhar (2014), and Jackson et al. (2014). Probes built for several particle size ranges were
69 examined, but those of interest here are cloud particle probes: the 2D-S and the older Two-Dimensional Cloud
70 (2DC) probe. Three particular results distilled from those papers are useful here.

71 First, a posteriori shattered particle removal is more effective at reducing counts of apparent shattering
72 fragments for the 2D-S than are modified probe tips, which result jibes with Lawson (2011). The opposite is true for
73 the 2DC. This is attributed to the 2D-S' larger sample volume and improvements in resolution and time response
74 over the 2DC (Jensen et al., 2009; Lawson, 2011), which allow it to size particles smaller than 100 μm and to
75 measure particle inter-arrival times more accurately (Lawson et al., 2010; Korolev et al., 2013b).

76 Second, shattered artifacts seem mainly to corrupt particle size bins less than about 500 microns. Thus
77 Korolev et al. (2013b) posit that bulk quantities computed from higher order PSD moments, such as shortwave
78 extinction coefficient, IWC, and radar reflectivity, are likely to compare much better between the 2D-S and the 2DC
79 than is N_T .

80 Third, the efficacy of shattered particle removal from the 2DC is questionable: post-processing is prone to
81 accepting shattered particles and to rejecting real particles (Korolev and Field, 2015). The parameters of the
82 underlying Poisson model and its ability to correctly identify shattered fragments depend on the physics of the cloud
83 being sampled (Vidaurre and Hallett, 2009; Korolev et al., 2011). Issues with instrument depth-of-field, unfocused
84 images, and image digitization further compound uncertainty (Korolev et al., 2013b; Korolev and Field, 2015).

85 In the context of relatively small studies such as these, Korolev et al. (2013b) pose two questions: “(i) to
86 what extent can the historical data be used for microphysical characterization of ice clouds, and (ii) can the historical
87 data be reanalyzed to filter out the data affected by shattering?” One difficulty in addressing these questions is the



88 scarcity of data from side-by-side instrument comparisons. Another is that, especially for the 2DC, “correcting
89 [data] a posteriori is not a satisfactory solution” (Vidaurre and Hallet, 2009). However, shattered particle removal is
90 the main (if not the only) correction method available when revisiting historical datasets.

91 As a start, though, Korolev et al.’s (2013b) first question is here addressed in terms of bulk cloud
92 properties, using shatter-corrected 2D-S data. Two points are critical to recall. First, the 2D-S is reasonably
93 expected to give results superior to the 2DC after shattered particle removal. Second, lingering uncertainty
94 notwithstanding, results presented elsewhere from the shatter-corrected 2D-S reveal behaviors in ice microphysics
95 within different regions of cloud that are expected both from physical reasoning and from modeling studies and that
96 were not always discernible before from in situ datasets (Lawson, 2011; Schwartz et al., 2017a).

97 To this end, a substantial climatology of shatter-corrected, 2D-S-measured cirrus PSDs is indirectly
98 compared with two large collections of older datasets, collected from the early 1990s through the mid-2000s mainly
99 using Particle Measurement Systems 2DC and Two-Dimensional Precipitation (2DP) probes (Baumgardner, 1989)
100 as well as Droplet Measurement Technologies Cloud- and Precipitation-Imaging Probes (CIP and PIP; Heymsfield
101 et al., 2009), and in one instance, the 2D-S. The older datasets are presented and parameterized in Delanoë et al.
102 (2005; hereinafter D05) and in Delanoë et al. (2014; hereinafter D14). The data used in D05 were not subject to
103 shattered particle removal, whereas the data in D14 were a posteriori.

104 The D05/D14 parameterizations take PSD moments as inputs and output parameterized 2DC PSDs. So, to
105 make the comparison, requisite moments from the 2D-S data are applied to the D05/D14 models in order to simulate
106 what the shatter- and non-shatter-corrected 2DCs would have measured had they flown with the 2D-S. A similarly
107 parameterized version of what the 2D-S actually measured is computed in order to make a fair comparison. It is
108 then seen whether the older datasets differ statistically from the newer via derived cirrus bulk properties.

109 Section 2 contains a description of the data used herein. Section 3 discusses the fitting of PSDs with
110 gamma distributions for computational use, Section 4 discusses the normalization and parameterization schemes
111 used by D05/D14, and Section 5 discusses the effects of not having included precipitation probe data with the 2D-S
112 data. Section 6 demonstrates the final results of the comparison.

113 **2 Data**

114 The 2D-S data was collected during the Mid-Latitude Airborne Cirrus Experiment (MACPEX), based in
115 Houston, TX during February and March, 2011 (MACPEX Science Team, 2011); the Small Particles in Cirrus



116 (SPartICus) campaign, based in Oklahoma during January through June, 2010 (SPartICus Science Team, 2010); and
117 TC⁴, based in Costa Rica during July, 2007 (TC⁴ Science Team, 2007). The SPEC 2D-S probe (Lawson, 2011)
118 images ice crystal cross-sections via two orthogonal lasers that illuminate two corresponding linear arrays of 128
119 photodiodes. PSDs, as well as distributions of cross-sectional area and estimated mass, are reported every second in
120 128 size bins with centers starting at 10 microns and extending out to 1280 microns. Particles up to about three
121 millimeters can be sized in one dimension by recording the maximum size along the direction of flight. During
122 SPartICus the 2D-S flew aboard the SPEC Inc. Learjet, while during MACPEX it was mounted on the NASA WB57
123 aircraft. During TC⁴ it was mounted on both the NASA DC8 and the NASA WB57, but the WB57 data is not used
124 due to documented contamination of the data from shattering artifacts off of the aircraft wing (Jensen et al., 2009).

125 Temperature was measured during MACPEX, TC⁴, and SPartICus using a Rosemount total temperature
126 probe. Bulk IWC measurements are available for MACPEX from the Closed-path tunable diode Laser Hygrometer
127 (CLH) probe (Davis et al., 2007). Condensed water that enters the CLH is evaporated so that a measurement of total
128 water can be made. The condensed part of the total water measured by the CLH is obtained by estimating
129 condensed water mass from concurrent PSDs measured by the National Center for Atmospheric Research (NCAR)
130 Video Image Particle Sampler (VIPS) probe and then subtracting this estimate from the measured total water mass.

131 3 Parametric Fitting of PSDs

132 PSDs measured by the 2D-S were fit with both unimodal and bimodal parametric gamma distributions.
133 The unimodal distribution is

$$134 \quad n(D) = N_0 \left(\frac{D}{D_0} \right)^\alpha \exp\left(-\frac{D}{D_0} \right), \quad (1)$$

135 where D is particle maximum dimension, D_0 is the scale parameter, α is the shape parameter, and N_0 is the so-called
136 intercept parameter. The bimodal distribution is simply a mixture of two unimodal distributions:

$$137 \quad n(D) = N_{01} \left(\frac{D}{D_{01}} \right)^{\alpha_1} \exp\left(-\frac{D}{D_{01}} \right) + N_{02} \left(\frac{D}{D_{02}} \right)^{\alpha_2} \exp\left(-\frac{D}{D_{02}} \right). \quad (2)$$

138 Save in a handful of instances (which will be indicated), all bulk PSD quantities shown here are computed using
139 these parametric fits. A combination of unimodal and bimodal fits is used to compute N_T , dictated by the shape of
140 the PSD as determined by a generalized chi-squared goodness of fit test (Schwartz et al., 2017b). Unimodal fits are
141 used to compute all other bulk quantities.



142 Unimodal fits were performed via the method of moments [in a manner similar to Heymsfield et al.
143 (2002)]. Both the method of moments and an expectation maximization algorithm (Moon, 1996; see the Appendix)
144 were used for the bimodal fits; the more accurate of those two fits [as determined by whether fit provided the
145 smaller binned Anderson-Darling test statistic (Demortier, 1995)] being kept.

146 Measured PSDs are both truncated and time-averaged in order to mitigate counting uncertainties. It is here
147 assumed that temporal averaging sufficiently reduces Poisson counting noise so that it may be ignored [see, e.g.,
148 Gayet et al. (2002)]. Given already cited concerns regarding uncertainty in shattered particle removal, the smallest
149 size bins are not automatically assumed here to be reliable. Other competing uncertainties further complicate
150 particle counts within the first few size bins, e.g., the possible underestimation of counts of real particles by a factor
151 of 5-10 (Gurganus and Lawson, 2016) and mis-sizing of larger drops into smaller size bins due to image break-up at
152 the edge of the instrument's depth of field (Korolev et al., 2013b; Korolev and Field, 2015).

153 In order to determine how many of the smallest size bins to truncate and for how many seconds to average
154 in order to make the counting assumption valid, two simple exercises were performed using the MACPEX dataset.
155 In the first exercise, fifteen-second temporal averages were performed along with truncating zero through two of the
156 smallest size bins while only the unimodal fits (chosen according to a maximum likelihood ratio test [Wilks, 2006])
157 were kept. Figure 1 shows comparisons of distributions of measured and computed (from the fits) N_T s. The
158 difference in the number of samples of computed N_T between zero bins and one bin truncated is an order of
159 magnitude higher than that between one bin and two bins truncated. This is due to frequent, extraordinarily high
160 numbers of particles recorded in the smallest size bin that at times cause a PSD to be flagged as bimodal by the
161 maximum likelihood ratio test. As this effect lessens greatly after truncating only one bin, and as the computed and
162 measured N_T s are otherwise better matched using a single-bin truncation, the smallest size bin is ignored for all
163 PSDs (making the smallest size bin used 15-25 microns).

164 Also, IWC was estimated from the fit distributions (the first size bin having been left off in the fits) using
165 the mass-dimensional relationship $m(D) = 0.0065D^{2.25}$ (m denotes mass, and all units are cgs) given in
166 Heymsfield (2003) for mid-latitude cirrus. The distribution of IWC thus computed nominally matches (not shown)
167 IWC estimates from both the CLH and from the 2D-S data product, which uses mass-projected area relationships
168 (Baker and Lawson, 2006).

169 For the second exercise, temporal averages from one to 20 seconds were performed, truncating the first size



170 bin and again keeping only the unimodal fits. The balance to strike in picking a temporal average length is
171 acceptably to smooth out Poisson counting uncertainties without losing physical information to an overlong average.
172 Qualitatively, the statistics of the fit parameters begin to steady at around 15 seconds (not shown), so a fifteen-
173 second temporal average was chosen. Using the data filters, temporal average, and bin truncation thus far described
174 results in ~17 000 measured PSDs and their accompanying fits.

175 It must be noted that the first 2D-S size bin contains at least some real particles, though the afore-
176 mentioned uncertainties make it impossible (at present) to know how many. Therefore, N_{TS} computed from the
177 remaining bins are perforce underestimations. Parametric fits extrapolate the binned data all the way to size zero,
178 though; so it could be assumed, if the real ice particle populations are in fact gamma-distributed, that this
179 extrapolation is a fair estimate of the real particles lost due to truncating the first size bin. In truth, however, the
180 assumption of a gamma-shaped PSD is arbitrary, if convenient; and even the assumption of Poisson counting
181 statistics, in the face of the artifacts mentioned in this paper, may be unwarranted. It is therefore felt that the
182 averaging approach is justified. The gamma PSD shape is kept for its convenience and for its ability to reproduce
183 higher-order PSD moments. However, in this paper, where N_{TS} (equivalently, the zeroth moments) from either the
184 parametric, the binned, or the normalized parametric PDSs are computed, the computations are begun at the left
185 edge of the second size bin so as to compare equivalent quantities. Thus, total number concentrations presented for
186 comparison here are truncated to compensate for having left off the smallest size bin.

187 4 Normalization and Parameterization

188 Each 2D-S-measured PSD $n_D(D)$, whose independent variable is ice particle maximum dimension, is
189 transformed to a distribution $n_{D_e}(D_e)$ whose independent variable is equivalent melted diameter. The
190 transformations are performed twice: once using the density-dimensional relationship used in D05 and once using a
191 mass-dimensional relationship used in D14.

192 The density-dimensional relationship $\rho(D) = aD^b$ (ρ denotes density, D denotes particle maximum
193 dimension, $a = 0.0056$, $b = -1.1$, and all units are cgs) used in D05 stems from relationships published by
194 Locatelli and Hobbs (1974) and Brown and Francis (1995) for aggregate particles. Setting masses equal as in D05
195 results in the independent variable transformation



196

$$D_e = \left(\frac{aD^b}{\rho_w} \right)^{1/3} D, \quad (3)$$

197 where ρ_w is the density of water.

198 The mass-dimensional relationship labeled “Composite” (Heymsfield et al., 2010) in D14 is used here for
 199 the second transformation:

200

$$m(D) = 7e^{-3} D^{2.2}.$$

201 (All units are again cgs.) Setting masses equal results in the independent variable transformation

202

$$D_e = \left(\frac{6a_{mi}}{\pi\rho_w} \right)^{1/3} D^{b_{mi}/3}. \quad (4)$$

203 The “composite” relation was only used to normalize about 54% of the PSD’s utilized in D14; however, those
 204 datasets so normalized are broadly similar to MACPex, SPARTICUS, and TC⁴ (one in fact is TC⁴, where the Cloud
 205 Imaging Probe was used as well as the 2D-S), and so the “composite” relation is used here for comparison with D14.

206 Following D05/D14s’ notation, transformed PSDs then have their independent variable scaled by mass-
 207 mean diameter

208

$$D_m = \frac{\int_0^\infty D_e^4 n_{D_e}(D_e) dD_e}{\int_0^\infty D_e^3 n_{D_e}(D_e) dD_e} \quad (5)$$

209 and their ordinates scaled by

210

$$N_0^* = \frac{4^4}{\Gamma(4)} \frac{\left[\int_0^\infty D_e^3 n_{D_e}(D_e) dD_e \right]^5}{\left[\int_0^\infty D_e^4 n_{D_e}(D_e) dD_e \right]^4}, \quad (6)$$

211 so that

212

$$n_{D_e}(D_e) = N_0^* F\left(x = \frac{D_e}{D_m}\right). \quad (7)$$

213 In Eq. (7), $F(x)$ is, ideally, the universal, normalized PSD (Meakin, 1992; Westbrook et al., 2004a,b; D05; Tinel
 214 et al., 2005; D14).



215 Having binned PSDs, the normalization procedure is wended as described in section 4.1 of D05. First, the
 216 2D-S bin centers and bin widths are transformed once using Eq. (3) for the comparison with D05 and once again
 217 using Eq. (4) for the comparison with D14. Next, each binned PSD is transformed by scaling from D -space to D_e -
 218 space (see below). Then, via numerically computed moments, Eqs. (5)-(7) are used to normalize the binned, mass-
 219 equivalent spherical PSDs, which are then grouped into normalized diameter bins of $\Delta x_i = 0.10$.

220 The scale factor for transformation is derived based on this simple consideration: if the number of particles
 221 within a size bin is conserved upon the bin's transformation from D -space to D_e -space, then, given that the
 222 transformation is from maximum dimension to mass-equivalent spheres, so also is the mass of the particles within a
 223 size bin conserved. That is,

$$224 \quad n_{D_e}(D_{e_i}) = n_D(D_i) \frac{a D_i^{b+3} \Delta D_i}{\rho_w D_{e_i}^3 \Delta D_{e_i}} \quad (8)$$

225 for the D05 transformation and

$$226 \quad n(D_{e_i}) = n(D_i) \frac{a_m D_i^{b_m} \Delta D_i}{\left(\frac{\pi}{6}\right) \rho_w D_{e_i}^3 \Delta D_{e_i}} \quad (9)$$

227 for the D14 transformation.

228 Mass-equivalent transformations theoretically ensure that both N_T and IWC can be obtained by using the
 229 PSD in either form:

$$230 \quad N_T = \int_0^\infty n_D(D) dD = \int_0^\infty n_{D_e}(D_e) dD_e \quad (10)$$

$$231 \quad \text{IWC} = \frac{\pi}{6} \int_0^\infty a D^{b+3} n_D(D) dD = \frac{\pi}{6} \int_0^\infty \rho_w D_{e_i}^3 n_{D_e}(D_e) dD_e \quad (11)$$

232 As it turns out, scaling from D -space to D_e -space so that Eqs. (10) and (11) are both satisfied is not necessarily
 233 possible. Since for the sake of estimating D_m and N_0^* it is more important that the IWCs be matched, this was done
 234 for the D05 comparison while matching the N_T s to within a factor of approximately 0.75, plus a bias of $\sim 3.1 \text{ L}^{-1}$.

235 The following transformation of variables must be used for computing other bulk quantities from
 236 transformed PSDs (Bain and Englehardt, 1992):



237
$$n_D(D) = n_{D_e} [D_e(D)] \left| \frac{dD_e}{dD} \right|. \quad (12)$$

238 For instance, effective radar reflectivity is computed using a set of power-law fits of T-matrix computations of
 239 backscatter cross section to particle maximum dimension (Matrosov, 2007; Matrosov et al., 2012; Posselt and Mace,
 240 2013; Hammonds et al., 2014) as follows:

241
$$Z_e = \frac{10^8 \lambda^4}{|K_w|^2 \pi^5} \sum_i \int_{D_i}^{D_{i+1}} a_{zi} D^{b_{zi}} n_{D_e} [D_e(D)] \left| \frac{dD_e}{dD} \right| dD.$$

242 The coefficients (a_{zi}, b_{zi}) were derived assuming an air/ice dielectric mixing model and that all particles are prolate
 243 spheroids with aspect ratios of 0.7 (Korolev and Isaac, 2003; Westbrook et al., 2004a; Westbrook et al., 2004b;
 244 Hogan et al., 2012). Several explicit expressions for computing bulk quantities based on equivalent distributions
 245 may be found in Schwartz (2014).

246 In D05/D14, data taken with cloud particle and precipitation probes were combined to give PSDs ranging
 247 from 25 μm to several millimeters. No precipitation probe data is used here, but how does not including
 248 precipitation probe data affect the comparison? This question will be addressed later in this paper.

249 Two-dimensional histograms of the normalized PSD are shown in Fig. 2 for the D05 transformation and in
 250 Fig. 4 for the D14 transformation, overlaid with their mean normalized PSDs (cf. Figs. 1 and 2 in D05 and Fig. 3 in
 251 D14). For both transformations, the mean normalized PSDs for the three datasets combined are repeated in Figs. 3
 252 and 5 as solid curves (cf. Fig. 3 of D05 and Fig. 6 of D14). These serve as the empirical universal, normalized PSDs

253 $F_{\sim 2DS-D05}(x)$ and $F_{\sim 2DS-D14}(x)$, derived using the mass transformations of D05 and D14, respectively. They,
 254 and the quantities derived therefrom, serve to represent the more modern 2D-S with shattered particle removal. The
 255 subscripts $\sim 2DS-D05$ and $\sim 2DS-D14$ are used hereinafter to represent bulk quantities derived using $F_{\sim 2DS-D05}(x)$
 256 and $F_{\sim 2DS-D14}(x)$.

257 Three parametric functions for $F(x)$ are given in D05, two of which are repeated here: the gamma- μ
 258 function (F_μ) and the modified gamma function ($F_{\alpha,\beta}$; Petty and Huang, 2011).



$$259 \quad F_{\mu}(x) = \frac{\Gamma(4)(4+\mu)^{4+\mu}}{4 \Gamma(4+\mu)} x^{\mu} \exp[-(4+\mu)x] \quad (13)$$

$$260 \quad F_{\alpha,\beta}(x) = \beta \frac{\Gamma(4) \Gamma\left(\frac{\alpha+5}{\beta}\right)^{4+\alpha}}{4^4 \Gamma\left(\frac{\alpha+4}{\beta}\right)^{5+\alpha}} x^{\alpha} \exp\left[-\frac{\left(\Gamma\left(\frac{\alpha+5}{\beta}\right)\right)^{\beta}}{\Gamma\left(\frac{\alpha+4}{\beta}\right)}\right] \quad (14)$$

261 Values of μ , α , and β can be chosen to fit these functions to a mean normalized PSD. In D05, the parametric
 262 functions $F_{\alpha,\beta} = F_{(-1,3)}$ (Eq. (14)) and $F_{\mu} = F_3$ (Eq. (13)) are given to approximate the universal PSD derived
 263 from combined 2DC-2DP datasets; and in D14, the parametric function $F_{\alpha,\beta} = F_{(-0.262,1.754)}$ is given to
 264 approximate the universal PSD derived from shatter-corrected datasets collected mainly with combined 2DC-2DP
 265 probes.

266 These functions are used to parameterize transformed PSDs measured by the 2DC-2DP, given two PSD
 267 moments. We therefore make the assumption that if we take the same two moments derived from a 2D-S-measured
 268 PSD and then apply them to Eq. (13) or (14), we have effectively simulated the transformed PSD that a combined
 269 2DC-2DP would have observed had they been present with the 2D-S. The subscripts $\sim 2DC(u)$ and $\sim 2DC(s)$ are
 270 used hereinafter to represent quantities that simulate 2DC-2DP data (non-shatter-corrected and shatter-corrected,
 271 respectively) in this way. Initial observations on comparison of $F_{\sim 2DS-D05}(x)$ and $F_{\sim 2DS-D14}(x)$ with the
 272 normalizations of D05 and D14 will now be given.

273 4.1 Comparison with D05

274 Right off the bat, some important qualitative observations can be made from examining $F_{\sim 2DS-D05}(x)$ in
 275 Fig. 3. First, in contrast to Fig. 3 of D05, the concentrations of particles at the smallest scaled diameters of
 276 $F_{\sim 2DS-D05}(x)$ are, on average, about an order of magnitude or more lower. From this it is surmised that while the
 277 2D-S continues to register relatively high numbers of small ice particles, the number has decreased in the newer
 278 datasets due to the exclusion of shattered ice crystals.

279 It can also be seen in Fig. 3 that the shoulder in the normalized PSDs in the vicinity of $x \sim 1.0$ exists in the



280 newer data as it does in the data used in D05. It is worth noting, though, that the shoulder exists in the one tropical
281 dataset used here (TC⁴), whereas it is absent or much less noticeable in the tropical datasets used in D05.

282 Fortuitously, $F_{\alpha,\beta} = F_{(-1,3)}$ fits the 2D-S data better than it does the older data at the smallest normalized
283 sizes (cf. Fig. 2 in D05). Neither $F_{\alpha,\beta} = F_{(-1,3)}$ nor $F_{\mu} = F_3$ correctly catches the shoulder in the newer data,
284 though $F_{\alpha,\beta} = F_{(-1,3)}$ was formulated to (better) catch a corresponding shoulder in the older data.

285 Next, a comparison of PSD quantities computed directly from the 2D-S with corresponding \sim 2DC-derived
286 quantities (computed using N_0^* and D_m derived directly from the binned 2D-S data and applied to $F_{\alpha,\beta} = F_{(-1,3)}$
287 and $F_{\mu} = F_3$) is made. The extinction coefficient, IWC, and 94 GHz radar reflectivity compare well between the
288 2D-S and both versions of \sim 2DCu (not shown). 2D-S and \sim 2DCu radar reflectivities have a slightly skewed and
289 slightly non-one-to-one relationship (this is an important consideration in the parameterization of N_0^* by Z given in
290 D05). As for N_T , it is the least certain computation (see Fig. 6); but $F_{\mu} = F_3$ is entirely wrong in attempting to
291 reproduce this quantity, so this shape is not used hereinafter and $F_{\sim 2DCu}(x) = F_{(-1,3)}(x)$ is the shape used to
292 simulate the uncorrected 2DC-2DP.

293 Figure 7 shows the mean relative error and the standard deviation of the relative error (cf. Fig. 5 of D05)
294 between 2D-S-derived and corresponding \sim 2DCu-derived quantities. (Effective radius is as defined in D05, and 2D-
295 S estimates of N_T here stem from truncated, binned data). Mean relative error for both extinction coefficient and
296 IWC is about -0.1%. The mean relative error in N_T (N_T computed directly from binned PSDs is used both here and
297 in Fig. 8) is rather large at \sim 50%; and the mean relative error in Z_e , at \sim 22%, is larger than that shown in Fig. 5 of
298 D05 (less than 5% there) but, at about 2 dB, is within the error of most radars. This may well be due to the
299 overestimation of $F(x)$ by $F_{\sim 2DCu}(x)$ between normalized sizes of about 1.2 and 2 [see Fig. 3b]. Both here and
300 in D05, $F_{\sim 2DCu}(x)$ falls off much more rapidly than $F(x)$ above a normalized diameter of two. However, it is
301 deduced from Figs. 2 and 5 in D05 that this roll-off is not responsible for the large mean relative error in Z shown in
302 Fig. 7.

303 The mean relative error in effective radius shown in Fig. 7 is approximately -7%, whereas it is apparently



304 nil in Fig. 5 of D05. Effective radius is defined in D05 as the ratio of the third to the second moments of the
305 spherical-equivalent PSDs and is therefore a weighted mean of the PSD. The negative sign on the relative error
306 indicates that, on average, $F_{-2DCu}(x)$ is underestimating the effective radius of the PSDs measured by the 2D-S
307 whereas for the older datasets it hits the effective radius spot-on (in the average). Therefore, there is a significant
308 difference between the 2D-S datasets and the older 2DC-2DP datasets in the ratio of large particles to small
309 particles, even when precipitation probe data is not combined with the 2D-S.

310 4.2 Comparison with D14

311 From Fig. 4, concentrations at the smallest scaled diameters of $F_{-2DS-D14}(x)$ are nominally consistent
312 with those shown in Fig. 6 of D14. In accordance with the surmise made in the comparison with D05 above, it
313 would seem that shattered particle removal from the 2DC improves comparison between the 2D-S and the 2DC-2DP
314 at the smallest particle sizes.

315 Here, $F_{-2DCs}(x) = F_{(-0.262, 1.754)}(x)$. The shoulder in the normalized PSDs in the vicinity of $x \sim 1.0$ is
316 again found, though the shoulder is not captured by $F_{-2DCs}(x)$ (see Fig. 5). The normalized 2D-S at the smallest
317 normalized sizes is also underestimated by $F_{-2DCs}(x)$. Comparison of N_T computed using $F_{-2DCs}(x)$ with that
318 derived from 2D-S is quite similar to that of $F_{-2DCu}(x)$ (not shown).

319 As shown in Fig. 8, the mean relative error between N_T and effective radius derived from the 2D-S and
320 from $\sim 2DCs$ is again about 50%, while the mean relative error in effective radius remains about -7.5%. The mean
321 relative error in reflectivity has decreased to about 14%.

322 5 Impact of Not Using Precipitation Probe Data

323 To more formally investigate the impact of not using a precipitation probe, data from the PIP were
324 combined with data from the 2D-S using the TC⁴ dataset. This campaign of the three was chosen due to its tending
325 to occur at warmer temperatures, in a more convective environment, and at lower relative humidities: so, if large
326 particles are going to matter, they should matter for TC⁴. Figure 9 shows, similar to Figs. 3 and 5, $F_{-2DS-D05}(x)$
327 for the 2D-S alone, $F_{-2DS-D05}(x)$ for the 2D-S combined with the PIP, and $F_{-2DCu}(x)$.

328 In the combined data, the average, normalized PSD does not dig as low between zero and unity as for the



329 2D-S alone; but it does show similar numbers of particles at the very smallest normalized sizes, and the shoulder is
 330 in the same location. Beginning at about $x = 1.2$, the 2D-S-PIP normalized distribution is higher than the 2D-S-
 331 alone normalized distribution; and it continues out to about $x = 10$, whereas the 2D-S-alone distribution ends shy of
 332 $x = 5$. In either case, $F_{-2DCu}(x)$ misses what is greater than about $x = 2$. This roll-off, along with the fact that the
 333 mean normalized and transformed 2D-S/PIP combination appears to be more similar to $F_{-2DS-D05}(x)$ than it does
 334 to $F_{-2DCu}(x)$, indicate that a parameterization of $F(x)$ based off the 2D-S alone is comparable to the 2DC/2DP-
 335 based $F_{-2DCu}(x)$ parameterization.

336 In support of this assertion, Fig. 10 shows the penalty in radar reflectivity, computed directly from data
 337 using the approach described earlier, incurred by using only the 2D-S instead of the 2D-S-PIP. The penalty is in the
 338 neighborhood of 1 dB.

339 The true N_0^* and D_m computed from each of the 2D-S PSDs alone and from the combined PSDs from
 340 TC⁴ were used, along with $F_{-2DCu}(x)$, to compute N_T , extinction coefficient, IWC, and 94 GHz effective radar
 341 reflectivity. This amounts to two different $\sim 2DCu$ simulations: one including the PIP and one not. The results are
 342 shown in Fig. 11. The distributions are very similar, with the exception of the reflectivity distributions, whose
 343 means are separated by less than 1 dBZ. It is concluded that the cloud filtering technique has resulted in PSDs that
 344 are satisfactorily described by the 2D-S alone, at least in the case of this comparison.

345 6 Final Results and Discussion

346 In D05, complete parameterization of a 2DC-2DP-measured PSD is achieved by using a universal shape
 347 $F_{\alpha,\beta}(x)$ along with N_0^* parameterized by radar reflectivity and D_m parameterized by temperature. For
 348 comparison with the shattered-corrected D14 study, a temperature-based parameterization of “composite”-derived
 349 D_m is also derived from the 2D-S data and “composite”-derived N_0^* is parameterized by radar reflectivity. A
 350 similar parameterization scheme (also based on radar reflectivity and temperature) for the 2D-S (based on Field et
 351 al., 2005) is outlined in Schwartz et al. (2017c) and is used here to compute a fully parameterized version of 2D-S-
 352 measured PSDs so as to make a fair comparison of them with fully parameterized 2DC-measured PSDs.

353 Figure 12 shows the results of computing PSD-based quantities using the fully parameterized 2D-S (red,



354 labeled “ $x2DS$ ”), the fully parameterized (uncorrected) 2DC (blue, labeled “ $x2DCu$ ”), and directly from the 2D-S
355 data (black). Probability density functions (pdfs) of 94 GHz effective radar reflectivity match because they are
356 forced to by the two instrument parameterizations. Otherwise, biases exist between the two sets of computations
357 based on simulated instruments and computations based on the actual 2D-S (black curve). This bias is due mainly to
358 the temperature parameterization of D_m . The pdfs of extinction coefficient and IWC for the two parameterized
359 instruments match one another quite well (the differences in their medians are not statistically significant).
360 However, for N_T , the $x2DCu$ pdf is shifted to higher concentrations than the pdf for $x2DS$. The difference in their
361 medians is statistically significant at the 95% level according to a Mann-Whitney U test. It is therefore concluded
362 that the older D05 parameterization based on the 2DC-2DP data sets predicts a statistically significant higher
363 number of total ice crystals than does the parameterized 2D-S (by a factor of about 1.3, or a little over 1 dB) and
364 that, more generally, the 2DC measures a larger ratio of small ice crystals to large ice crystals than does the 2D-S, as
365 shown in the effective radius comparison in Fig. 7.

366 Figure 13 shows pdfs of N_T and extinction coefficient computed using the fully parameterized 2D-S (red,
367 labeled “ $x2DS$ ”), the fully parameterized (corrected) 2DC (blue, labeled “ $x2DCs$ ”), and directly from the 2D-S data
368 (black). The pdfs of extinction match quite well, but their medians are significantly different according to the U test.
369 The medians of N_T are also significantly different, but the mean of the parameterized, corrected 2DC is lower than
370 that of the parameterized 2D-S. A posteriori shatter correction has made 2DC measurements more like 2D-S
371 measurements in the bulk quantity of total particle concentration, however, a statistically significant difference
372 between the 2D-S and the corrected 2DC remains. This result is entirely expected in light of the previous results
373 outlined in the introduction to this paper.

374 Via an indirect comparison to older, 2DC-based datasets by means of parameterizations given in D05 and
375 in D14, it is determined that the 2D-S cirrus cloud datasets used here are significantly different from historical
376 datasets in numbers of small ice crystals measured. Furthermore, it is determined that were a 2DC to have been
377 flown alongside a 2D-S during MACPEX, SPaRtICus, and TC^d, the 2DC would have reported significantly higher
378 numbers of the smallest ice crystals. Were a posteriori shattered particle removal applied to the 2DC data the total
379 numbers of ice crystals measured by the 2D-S and 2DC would have become more similar, but N_T measured by the
380 2DC would remain statistically different from that measured by the 2D-S.

381 Our aim was to determine whether the historical data sets analyzed by D05 and D14 continue to be



382 scientifically viable given the newer probes and modern processing techniques. Given the modest differences found
383 here between the newer and older data, we conclude that the historical data sets do indeed continue to be useful with
384 the caveats noted above. However, it is surmised that, since the efficacy of a posteriori shatter correction on the
385 2DC is questionable and since the 2D-S is superior in response time, resolution, and sample volume to the 2DC, and
386 that since steps were taken to mitigate ice particle shattering in the 2D-S data, the newer datasets are more accurate.
387 Therefore, continuing large-scale field investigations of cirrus clouds using the newer particle probes and data
388 processing techniques are recommended and, where possible, investigation, by means of flying 2DC probes
389 alongside 2D-S probes, of the possibility of effecting statistical correction of historical cirrus ice particle datasets
390 using newer datasets.

391 It is important to note that this study does not specifically consider PSD shape. This is a critical component
392 of the answers to Korolov et al.'s (2013b) original two questions. Mitchell et al. (2011) demonstrated that for a
393 given effective diameter and IWC, the optical properties of a PSD are sensitive to its shape. Therefore, PSD
394 bimodality and concentrations of small ice crystals are critical to realistically parameterizing, cirrus PSDs, to
395 modeling their radiative properties and sedimentation velocities, and to mathematical forward models designed to
396 infer cirrus PSDs from remote sensing observations (Lawson et al., 2010; Mitchell et al., 2011; Lawson, 2011). We
397 therefore reiterate the need for ongoing, large-scale investigations of cirrus clouds that make use of advanced
398 imaging equipment, such as the 2D-S, flown alongside older instruments such as the 2DC. Thus, not only will new
399 measurements with up-to-date instruments be made, but the measurements necessary for the correction of historical
400 cirrus datasets will also be obtained.

401 **Data Availability**

402 All SPARTICus data may be accessed via the Atmospheric Radiation Measurement (ARM) data archive as
403 noted in the references. All MACPEX and TC⁴ data may be accessed from the NASA Earth Science Project Office
404 (ESPO) data archive, also noted in the references.

405 **ACKNOWLEDGEMENTS**

406 Thanks are given to Drs. Gerald G. Mace, Paul Lawson, and Andrew Heymsfield for helpful discussions
407 that led to significant improvement in the manuscript. This work was supported by the U.S. Department of Energy's
408 (DOE) Atmospheric System Research (ASR), an Office of Science, Office of Biological and Environmental
409 Research (BER) program, under Contract DE-AC02-06CH11357 awarded to Argonne National Laboratory. This



410 work was also supported by the National Science Foundation (NSF) Grant AGS-1445831. Grateful
 411 acknowledgement is also given to the computing resources provided on Blues, a high-performance computing
 412 cluster operated by the Laboratory Computing Resource Center (LCRC) at the Argonne National Laboratory.

413 **APPENDIX: Bimodal Fits using Expectation Maximization**

414 At the beginning, it is noted that this algorithm is effective at identifying and parameterizing multiple
 415 modes in binned ice PSD measurements made by a single instrument, but that it does not work well for PSDs that
 416 result from combining binned measurements of two different probes (as of the 2D-S and a precipitation probe.)
 417 Following Johnson et al. (2013), binned counts of cloud particles are modeled as independent samples taken from a
 418 multinomial distribution (Bain and Englehardt, 1992). Let y_l be the number of particle counts in the l^{th} size bin
 419 (from a total of L possible size bins). Thus, if the observed PSD is the vector \mathbf{y} , then its probability mass function
 420 (pmf) is

$$421 \quad \Pr(\mathbf{y}) = p_{\mathbf{y}}(\mathbf{y}) = \frac{N_T!}{\prod_{l=1}^L y_l!} \prod_{l=1}^L p_l^{y_l}, \quad (\text{A1})$$

422 where p_l is the probability of obtaining a count in the l^{th} size bin (computed by integrating Eq. (3)) and where N_T is
 423 the total number of counts.

424 Alternatively, binned counts can be modeled as samples from a multinomial distribution with $2L$ bins: a
 425 sample may fall in bin l_1 (small particle mode) or in bin l_2 (large particle mode). Let x_{l1} be the number of counts in
 426 the l^{th} small-mode size bin, and let x_{l2} be the number of counts in the l^{th} large-mode size bin. In this case, the pmf
 427 may be expressed in either of two forms:

$$428 \quad p_{\mathbf{x}_1, \mathbf{x}_2}(\mathbf{x}_1, \mathbf{x}_2) = \frac{N_T!}{\prod_{l=1}^L x_{l1}! x_{l2}!} \prod_{l=1}^L p_{l1}^{x_{l1}} p_{l2}^{x_{l2}}, \text{ or } (\text{A2})$$

$$429 \quad p_{\mathbf{x}_1, \mathbf{x}_2}(\mathbf{x}_1, \mathbf{x}_2) = \frac{N_T!}{\prod_{l=1}^L x_{l1}! x_{l2}!} \exp\left\{\sum_{l=1}^L x_{l1} \ln[p_{l1}] + x_{l2} \ln[p_{l2}]\right\}. \quad (\text{A3})$$

430 Here, p_{l1} is the probability of obtaining a count in the l^{th} size bin of the PSD's small mode and likewise for p_{l2} .
 431 These probabilities are computed by integrating the large and small modes of Eq. (4). For example,

$$432 \quad p_{l1} = \frac{\eta_1}{\Gamma(\alpha_1 + 1)} \left[\gamma\left(\alpha_1 + 1, \frac{D_{l+1}}{D_1}\right) - \gamma\left(\alpha_1 + 1, \frac{D_l}{D_1}\right) \right], \quad (\text{A4})$$



433 where $\gamma(\dots)$ is the lower incomplete gamma function.

434 This algorithm iterates through pairs of expectation and maximization steps. Following Moon (1996), we
 435 begin with the function

$$436 \quad Q(\boldsymbol{\theta}, \boldsymbol{\theta}^{[k]}) = E \left\{ \ln \left[p(\mathbf{x} | \boldsymbol{\theta}) | \mathbf{y}, \boldsymbol{\theta}^{[k]} \right] \right\}, \quad (\text{A5})$$

437 where $p(\mathbf{x}, \boldsymbol{\theta})$ denotes the likelihood function of the vector of mixture distribution parameters $\boldsymbol{\theta}$ given the
 438 (missing) data vector $\mathbf{x} = [\mathbf{x}_1 \ \mathbf{x}_2]$. For the expectation step, the expected value of the log-likelihood function is
 439 computed with respect to \mathbf{x} , given a set of observed data \mathbf{y} and a current estimate of the parameters $\boldsymbol{\theta}^{[k]}$. This
 440 expected value becomes the current estimate of the missing data $\mathbf{x}^{[k]}$. Equation (A5) is then maximized with respect
 441 to the parameter vector $\boldsymbol{\theta}$ in order to obtain a new estimate $\boldsymbol{\theta}^{[k+1]}$:

$$442 \quad \boldsymbol{\theta}^{[k+1]} = \arg \max_{\boldsymbol{\theta}} \left[Q(\boldsymbol{\theta}, \boldsymbol{\theta}^{[k]}) \right]. \quad (\text{A6})$$

443 As $p_{\mathbf{x}_1, \mathbf{x}_2}(\mathbf{x}_1, \mathbf{x}_2)$ belongs to the exponential distribution family, it suffices for the expectation step
 444 simply to estimate \mathbf{x}_1 and \mathbf{x}_2 (Moon, 1996). To do so, their expected values, conditioned upon the observations \mathbf{y}
 445 and on an estimate of the distribution parameters $\boldsymbol{\theta}^{[k]}$, are found. Equation (A6) is accordingly transformed so that

$$446 \quad p_{\mathbf{x}_1, \mathbf{y}}(\mathbf{x}_1, \mathbf{y}) = p_{\mathbf{x}_1, \mathbf{x}_2}(\mathbf{x}_1, \mathbf{y} - \mathbf{x}_1) = \frac{N_T!}{\prod_{l=1}^L x_{l1}! (y_l - x_{l1})!} \prod_{l=1}^L p_{l1}^{x_{l1}} p_{l2}^{(y_l - x_{l1})}. \quad (\text{A7})$$

447
 448 The conditional distribution of \mathbf{x}_1 is therefore

$$449 \quad p(\mathbf{x}_1 | \mathbf{y}) = \frac{p_{\mathbf{x}_1, \mathbf{y}}(\mathbf{x}_1, \mathbf{y})}{p_{\mathbf{y}}(\mathbf{y})} = \prod_{l=1}^L \frac{y_l!}{x_{l1}! (y_l - x_{l1})!} \left(\frac{p_{l1}}{p_l} \right)^{x_{l1}} \left(\frac{p_{l2}}{p_l} \right)^{(y_l - x_{l1})}, \quad (\text{A8})$$

450 which is the joint distribution of a sample of independent binomial random variables. Similarly, it may be found
 451 that

$$452 \quad p(\mathbf{x}_2 | \mathbf{y}) = \prod_{l=1}^L \frac{y_l!}{x_{l2}! (y_l - x_{l2})!} \left(\frac{p_{l1}}{p_l} \right)^{(y_l - x_{l2})} \left(\frac{p_{l2}}{p_l} \right)^{x_{l2}}. \quad (\text{A9})$$

453 The conditional expectations are therefore



454
$$E[x_{i1} | y_i] = x_{i1}^{[k]} = y_i \frac{p_{i1}^{[k]}}{p_i^{[k]}}, \text{ and } \quad (\text{A10})$$

455
$$E[x_{i2} | y_i] = x_{i2}^{[k]} = y_i \frac{p_{i2}^{[k]}}{p_i^{[k]}}. \quad (\text{A11})$$

456 The maximization step then requires maximizing the logarithm of Eq. (A3) with respect to θ , using the
 457 estimates $x_1^{[k]}$ and $x_2^{[k]}$. Dropping terms that are not functions of the distribution parameters gives

458
$$\theta^{[k+1]} = \arg \max_{\theta} \left\{ \sum_{i=1}^L x_{i1}^{[k+1]} \ln[p_{i1}] + x_{i2}^{[k+1]} \ln[p_{i2}] \right\}. \quad (\text{A12})$$

459 Equations (A10)-(A12) are iterated, using an initial estimate for the distribution parameters $\theta^{[0]}$ (see Schwartz,
 460 2014), until the distribution parameters converge.

461 Solutions for N_1 and N_2 come from the definition of η_1 and from the second non-central sample moment of
 462 the non-normalized PSD M_2 :

463
$$N_1 = \frac{\eta_1 M_2}{D_1 \Gamma(\alpha_1 + 1) [\eta_1 D_1^2 (\alpha_1 + 2)(\alpha_1 + 1) + (1 - \eta_1)(\alpha_2 + 2)(\alpha_2 + 1)]} \quad (\text{A14})$$

464
$$N_2 = \frac{(1 - \eta_1) M_2}{D_2 \Gamma(\alpha_2 + 1) [\eta_1 D_1^2 (\alpha_1 + 2)(\alpha_1 + 1) + (1 - \eta_1)(\alpha_2 + 2)(\alpha_2 + 1)]}. \quad (\text{A15})$$

465 The second non-central moment is used to ensure good reproduction of the zeroth through the second non-central
 466 PSD moments by the solution. The mode for which the product of the scale and shape parameters is the larger is
 467 selected as the large mode.

468 The log-likelihood function in Eq. (A5) has many local maxima so the iterative search for a global
 469 maximum is highly sensitive to the first guess given to it. The method for dealing with this problem is described in
 470 Schwartz (2014).

471 **Competing Interests**

472 The author declares that he has no conflict of interest.



473 REFERENCES

- 474 Bain, L. J. and M. Englehardt, 1992: *Introduction to Probability and Mathematical Statistics*,
475 *2nd Ed.* Duxbury Press, 644 pp.
476
- 477 Baker, B. A. and R. P. Lawson, 2006: Improvement in determination of ice water content from
478 two-dimensional particle imagery. Part I: Image-to-mass relationships. *J. Appl. Meteor. Climatol.*, **45**,
479 1282-1290.
480
- 481 Baumgardner, D., 1989: Airborne Measurements for Cloud Microphysics. *Res. Aviat. Facility*
482 *Bull.*, **24**, 1-22.
483
- 484 Brown, P. R. A., and P. N. Francis, 1995: Improved Measurements of the Ice Water Content in
485 Cirrus Using a Total Water Probe. *J. Atmos. Oceanic Technol.*, **12**, 410-414.
486
- 487 Cooper, W. A., 1978: Cloud physics investigations by the University of Wyoming in HIPLEX
488 1977. Department of Atmospheric Science, University of Wyoming, Rep. AS119, 320 pp.
489
- 490 Davis, S. M., A. G. Hallar, L. M. Avallone, and W. Engblom, 2007: Measurements of Ice Water
491 Content With a Tunable Diode Laser Hygrometer: Calibration Procedure and Inlet Analysis. *J. Atmos.*
492 *Oceanic Technol.*, **24**, 463, doi:10.1175/JTECH1975.1.
493
- 494 Delanoë, J., A. Protat, J. Testud, D. Bouniol, A. J. Heymsfield, A. Bansemer, P. R. A. Brown,
495 and R. M. Forbes, 2005: Statistical properties of the normalized ice particle size distribution. *J. Geophys.*
496 *Res.*, **110**, doi:10.1029/2004JD005405.
497
- 498 Delanoë, J. M. E., A. J. Heymsfield, A. Protat, A. Bansemer, and R. J. Hogan, 2014: Normalized
499 particle size distribution for remote sensing application. *J. Geophys. Res.*, **119**,
500 doi:10.1002/2013JD020700.
501
- 502 Demortier, Luc, 1995: Assessing the Significance of a Deviation in the Tail of a Distribution.
503 Collider Detector at Fermilab note 3419.
504
- 505 Field, P. R., 2000: Bimodal ice spectra in frontal clouds. *Quart. J. Roy. Meteor. Soc.*, **126**, 379-
506 392.
507
- 508 Field, P. R., R. Wood, P. R. A. Brown, P. H. Kay, E. Hirst, R. Greenaway, and J. A. Smith,
509 2003: Ice Particle Interarrival Times Measured with a Fast FSSP. *J. Atmos. Oceanic Technol.*, **20**, 249-
510 261.
511
- 512 Field, P. R., R. J. Hogan, P. R. A. Brown, A. J. Illingworth, T. W. Choullarton, and R. J. Cotton,
513 2005: Parameterization of ice-particle size distributions for mid-latitude stratiform cloud. *Quart. J. Roy.*
514 *Meteor. Soc.*, **131**, 1997-2017.
515
- 516 Field, P. R., A. J. Heymsfield, and A. Bansemer, 2006: Shattering and particle interarrival times
517 measured by optical array probes in ice clouds. *J. Atmos. Oceanic Technol.*, **23**, 1357-1371.
518
- 519 Gayet, J.-F., F. Auriol, A. Minikin, J. Stroem, M. Seifert, R. Krejci, A. Petzold, G.
520 Febvre, and U. Schumann, 2002: Quantitative measurement of the microphysical and optical properties of
521 cirrus clouds with four different in situ probes: Evidence of small ice crystals. *Geophys. Res. Lett.*, **29**,
522 doi:10.1029/2001GL014342.
523
- 524 Gayet, J.-F., J. Ovarlez, V. Shcherbakov, J. Stroem, U. Schumann, A. Minikin, F. Auriol,
525 A. Petzold, and M. Monier, 2004: Cirrus cloud microphysical and optical properties at southern and
526 northern midlatitudes during the INCA experiment. *J. Geophys. Res.*, **109**, D20206,
527 doi:10.1029/2004JD004803.



- 528
 529 Gayet, J.-F., V. Shcherbakov, H. Mannstein, A. Minikin, U. Schumann, J. Stroem, A.
 530 Petzgold, J. Ovarlez, and F. Immler, 2006: Microphysical and optical properties of midlatitude cirrus
 531 clouds observed in the southern hemisphere during INCA. *Quart. J. Roy. Meteor. Soc.*, **132**, 2719-2748.
 532
 533 Gurganus, C. and P. Lawson, 2016: Improvements in Optical Array Probe Characterization:
 534 Laboratory and Simulation Results. *XVII International Conference on Clouds and Precipitation*,
 535 Manchester, UK, the International Association of Meteorology and Atmospheric Sciences and the
 536 International Commission on Clouds and Precipitation.
 537
 538 Hammonds, K. D., G. G. Mace, and S. Y. Matrosov, 2014: Characterizing the Radar
 539 Backscatter-Cross-Section Sensitivities of Ice-Phase Hydrometeor Size Distributions via a Simple Scaling
 540 of the Clausius-Mossotti Factor. *J. Appl. Meteor. Climatol.*, **53**, 2761-2774.
 541
 542 Heymsfield, A. J., A. Bansemmer, P. R. Field, S. L. Durden, J. L. Stith, J. E. Dye, W. Hall, and C.
 543 A. Grainger, 2002: Observations and Parameterizations of Particle Size Distributions in Deep Tropical
 544 Cirrus and Stratiform Precipitating Clouds: Results from In Situ Observations in TRMM Field Campaigns.
 545 *J. Atmos. Sci.*, **59**, 3457-3491.
 546
 547 Heymsfield, A. J., 2003: Properties of Tropical and Midlatitude Ice Cloud Particle Ensembles.
 548 Part I: Median Mass Diameters and Terminal Velocities. *J. Atmos. Sci.*, **60**, 2573-3591.
 549
 550 Heymsfield, A. J., A. Bansemmer, G. Heymsfield, and A. O. Fierro, 2009: Microphysics of
 551 Maritime Tropical Convective Uprrafts at Temperatures from -20° to -60°C. *J. Atmos. Sci.*, **66**, 3530-3562.
 552
 553 Heymsfield, A. J. C. Schmitt, A. Bansemmer, and C. H. Twohy, 2010: Improved representation of
 554 ice particle masses based on observations in natural clouds, *J. Atmos. Sci.*, **67**, 3303-3318,
 555 doi:10.1175/2010JAS3507.1
 556
 557 Hobbs, P. V. and A. L. Rangno, 1985: Ice particle concentrations in clouds. *J. Atmos.*
 558 *Sci.*, **42**, 2523-2549.
 559
 560 Hogan, R. J., L. Tian, P. R. A. Brown, C. D. Westbrook, A. J. Heymsfield, and J. D. Eastment,
 561 2012: Radar Scattering from Ice Aggregates Using the Horizontally Aligned Oblate Spheroid
 562 Approximation. *J. Appl. Meteor. Climatol.*, **51**, 655-671.
 563
 564 Jackson, R. C. and G. M. McFarquhar, 2014: An Assessment of the Impact of Antishattering
 565 Tips and Artifact Removal Techniques on Bulk Cloud Ice Microphysical and Optical Properties Measured
 566 by the 2D Cloud Probe. *J. Atmos. Oceanic Technol.*, **30**, 2131-2144.
 567
 568 Jackson, R. C., G. M. McFarquhar, J. Stith, M. Beals, R. A. Shaw, J. Jensen, J. Fugal, and A.
 569 Korolev, 2014: An Assessment of the Impact of Antishattering Tips and Artifact Removal Techniques on
 570 Cloud Ice Size Distributions Measured by the 2D Cloud Probe. *J. Atmos. Oceanic Technol.*, **31**, 2576-
 571 2590.
 572
 573 Jensen, E. J., and Coauthors, 2009: On the importance of small ice crystals in tropical anvil
 574 cirrus. *Atmos. Chem. Phys.*, **9**, 5519-5537.
 575
 576 Johnson, R. W., D. V. Kliche, and P. L. Smith, 2013: Maximum likelihood estimation
 577 of gamma parameters for coarsely-binned and truncated raindrop size data. *Quart. J. Roy. Meteor. Soc.*,
 578 doi:10.1002/qj.2209.
 579
 580 Khain, A., M. Pinsky, T. Elperin, N. Kleeorin, I. Rogachevskii, and A. Kostinski, 2007:
 581 Critical comments to results of investigations of drop collisions in turbulent clouds. *Atmospheric Research*,
 582 **86**, 1-20.
 583



- 584 Korolev, A. V. and G. Isaac, 2003: Roundness and Aspect Ratio of Particles in Ice Clouds. *J.*
 585 *Atmos. Sci.*, **60**, 1795-1808.
- 586
 587 Korolev, A. V., E. F. Emery, J. W. Strapp, S. G. Cober, G. A. Isaac, M. Wasey, and D. Marcotte,
 588 2011: Small Ice Particles in Tropospheric Clouds: Fact or Artifact?. *Bull. Amer. Meteor. Soc.*, **92**, 967-
 589 973.
- 590
 591 Korolev, A., E. Emery, and K. Creelman, 2013a: Modification and Tests of Particle Probe Tips
 592 to Mitigate Effects of Ice Shattering. *J. Atmos. Oceanic Technol.*, **30**, 690-708.
- 593
 594 Korolev, A. V., E. F. Emery, J. W. Strapp, S. G. Cober, and G. A. Isaac, 2013b: Quantification
 595 of the effects of Shattering on Airborne Ice Particle Measurements. *J. Atmos. Oceanic Technol.*, **30**, 2527-
 596 2553.
- 597
 598 Korolev, A., and P. R. Field, 2015: Assessment of the performance of the inter-arrival time
 599 algorithm to identify ice shattering artifacts in cloud particle probe measurements. *Atmos. Meas. Tech.*, **8**,
 600 761-777.
- 601
 602 Kostinski, A. B., and R. A. Shaw, 2001: Scale-dependent droplet clustering in turbulent
 603 clouds. *J. Fluid. Mech.*, **434**, 389-398.
- 604
 605 Lawson, R. P., B. Baker, B. Pilson, and Q. Mo, 2006: In Situ Observations of the
 606 Microphysical Properties of Wave, Cirrus, and Anvil Clouds. Part II: Cirrus Clouds. *J. Atmos. Sci.*, **63**,
 607 3186-3203.
- 608
 609 Lawson, R. P., E. Jensen, D. L. Mitchell, B. Baker, Q. Mo, and B. Pilson, 2010: Microphysical
 610 and radiative properties of tropical clouds investigated in TC4 and NAMMA. *J. Geophys. Res.*, **115**,
 611 doi:10.1029/2009JD013017.
- 612
 613 Lawson, R. P., 2011: Effects of ice particles shattering on the 2D-S probe. *Atmos. Meas.*
 614 *Tech.*, **4**, 1361-1381.
- 615
 616 Locatelli, J. D., and P. V. Hobbs, 1974: Fall speed and masses of solid precipitation particles. *J.*
 617 *Geophys. Res.*, **79**, 2185-2197.
- 618
 619 MACPex Science Team, 2011: MACPEX. NASA Earth Science Project Office Data Archive, accessed 31 March
 620 2013. [Available online at <https://espoarchive.nasa.gov/archive/browse/macpex>.]
- 621
 622 Matrosov, S. Y., 2007: Modeling Backscatter Properties of Snowfall at Millimeter Wavelengths.
 623 *J. Atmos. Sci.*, **64**, 1727-1736.
- 624
 625 Matrosov, S. Y., G. G. Mace, R. Marchand, M. D. Shupe, A. G. Hallar, and I. B. McCubbin,
 626 2012: Observations of Ice Crystal Habits with a Scanning Polarimetric W-Band Radar at Slant Linear
 627 Depolarization Ratio Mode. *J. Atmos. Oceanic Technol.*, **29**, 989-1008.
- 628
 629 McFarquhar, G. M., J. Um, M. Freer, D. Baumgardner, G. L. Kok, and G. Mace, 2007:
 630 Importance of small ice crystals to cirrus properties: Observations from the Tropical Warm Pool
 631 International Cloud Experiment (TWP-ICE). *Geophys. Res. Lett.*, **34**, doi:10.1029/2007GL029865.
- 632
 633 Meakin, P., 1992: Aggregation kinetics. *Physica Scripta*, **46**, 295-331.
- 634
 635 Mitchell, D. L., R. P. Lawson, and B. Baker, 2011: Understanding effective diameter and its
 636 application to terrestrial radiation in ice clouds. *Atmos. Chem. Phys.*, **11**, 3417-3429.
- 637
 638 Moon, T. K., 1996: The Expectation-Maximization Algorithm. *IEEE Signal Processing*
 639 *Magazine*, **13**, 47-60.



- 640
 641 Petty, G. W. and W. Huang, 2011: The Modified Gamma Size Distribution Applied to
 642 Inhomogeneous and Nonspherical Particles: Key Relationships and Conversions. *J. Atmos. Sci.*, **68**, 1460-
 643 1473.
- 644
 645 Pinsky, M. and A. Khain, 2003: Fine structure of cloud droplet concentration as seen
 646 from the Fast-FSSP measurements. Part II: Results of in situ observations. *J. Appl. Meteor. Climatol.*, **42**,
 647 65–73.
- 648
 649 Posselt, D. and G. G. Mace, 2013: The Influence of Parameter Uncertainty on Snowfall
 650 Retrievals Using Markov Chain Monte Carlo Solution Methods. *J. Appl. Meteor. Climatol.*, Accepted.
- 651
 652 Schwartz, M. C., 2014: Analysis of Cirrus Particle Size Distributions from Three In Situ Flight
 653 Campaigns: Applications to Cirrus Microphysics and Parameterization, Remote Sensing, and Radar
 654 Forward Model Simulators. Ph.D. dissertation, Dept. of Atmospheric Sciences, the University of Utah, 229
 655 pp.
- 656
 657 Schwartz, M. C., G. G. Mace, R. P. Lawson, Q. Mo, T. P. Bui, G. S. Diskin, J. G. Anderson, and
 658 A. Avallone, 2017a: An Analysis of Bimodality in Cirrus Particle Size Distributions from the TC⁴,
 659 SPartICUs, and MACPEX Flight Campaigns. Submitted to *Atmospheric Chemistry and Physics*.
- 660
 661 Schwartz, M. C., G. G. Mace, R. P. Lawson, Q. Mo, T. P. Bui, G. S. Diskin, J. G. Anderson, and
 662 A. Avallone, 2017b: Statistics and A Priori Distributions of Cirrus Particle Size Distributions from the
 663 TC⁴, SPartICUs, and MACPEX Flight Campaigns. Submitted to *Atmospheric Chemistry and Physics*.
- 664
 665 Schwartz, M. C., G. G. Mace, R. P. Lawson, Q. Mo, T. P. Bui, G. S. Diskin, J. G. Anderson, and
 666 A. Avallone, 2017c: Parameterization of a Normalized, Universal Cirrus Particle Size Distribution Using
 667 the Two-Dimensional Stereo (2D-S) Probe. Submitted.
- 668
 669 SPartICus Science Team, 2010: SPartICus. Atmospheric Radiation Measurement Data Archive, PI/Campaign Data,
 670 accessed 26 March 2013. [Available online at
 671 <http://www.archive.arm.gov/discovery/#v/results/s/fiop::aaf2009Sparticus>.]
- 672
 673 TC⁴ Science Team, 2007: TC4 DC-8 files. NASA Earth Science Project Office Data Archive, accessed 29 March
 674 2012. [Available online at <https://espoarchive.nasa.gov/archive/browse/tc4/DC8>.]
- 675
 676 Tinel, C., J. Testud, J. Pelon, R. J. Hogan, A. Protat, J. Delanoe, and D. Bouniol, 2005:
 677 The retrieval of ice-cloud properties from cloud radar and lidar synergy. *J. Appl. Meteor.*, **44**, 860–875.
- 678
 679 Vidaurre, G. and J. Hallett, 2009: Particle Impact and Breakup in Aircraft Measurement. *J.*
 680 *Atmos. Oceanic Technol.*, **26**, 972–983.
- 681
 682 Westbrook, C. D., R. C. Ball, P. R. Field, and A. J. Heymsfield, 2004a: Universality in
 683 snowflake aggregation. *Geophys. Res. Lett.*, **31**, L15104, doi:10.1029/2004GL020363.
- 684
 685 Westbrook, C. D., R. C. Ball, P. R. Field, and A. J. Heymsfield, 2004b: Theory of growth by
 686 differential sedimentation, with application to snowflake formation. *Physical Review E*, **70**, 021403,
 687 doi:10.1103/PhysRevE.70.021403.
- 688
 689 Wilks, D. S., 2006: *Statistical Methods in the Atmospheric Sciences*, 2nd Ed. Academic Press,
 690 627 pp.
- 691
 692 Zhao, Y., G. G. Mace, and J. M. Comstock, 2011: The occurrence of particle size
 693 distribution bimodality in midlatitude cirrus as inferred from ground-based remote sensing data. *J. Atmos.*
 694 *Sci.*, **68**, 1162–1176.
- 695



696 **FIGURE CAPTIONS**

697

698 Figure 1: Comparisons of computed and measured total number concentration for 15-second PSD averages and for
699 truncation of none through the first two PSD size bins.

700

701 Figure 2: Histograms of normalized PSDs from each flight campaign, overlaid with their mean, normalized PSDs
702 (D05 normalization). The color map is truncated at 75% of the highest number of samples in a bin so as to increase
703 contrast. (a) TC⁴ (b) MACPEX (c) SPaRTICus (d) all data combined

704 Figure 3: The mean, normalized PSD (D05 normalization) from all three datasets combined, overlaid with two
705 parameterizations from D05: the gamma-mu parameterization (dash-dotted curve) and the modified gamma
706 parameterization (dashed curve). Panel (b) is a zoom-in on a portion of panel (a).

707 Figure 4: Same as Figure 2, but using D14 normalization.

708 Figure 5: The mean, normalized PSD (D14 normalization) from all three datasets combined, overlaid with the
709 parameterizations from D14. Panel (b) is a zoom-in on a portion of panel (a).

710

711 Figure 6: Total number concentration computed using the parameterized universal PSDs from D05 along with true
712 values of N_0^* and D_m (from the 2D-S data) scattered vs. total number concentration computed directly from
713 untransformed 2D-S data.

714

715 Figure 7: Mean relative error and standard deviation of the relative error between total number concentration
716 (divided by 10), effective radius, IWC, and Z as computed directly from the 2D-S and as computed from the
717 modified-gamma universal PSD shape and the true N_0^* and D_m computed from the 2D-S data.

718

719 Figure 8: As in Figure 7, but using the shatter-corrected 2DC parameterization.

720

721

722 Figure 9: Data from TC⁴ alone. The mean, normalized PSD from the 2D-S is overlaid with the mean, normalized
723 PSD obtained from combining the 2D-S with the PIP and the modified gamma parameterization from D05 (dashed
724 curve). Panel (b) is a zoom-in on a portion of panel (a).

725

726 Figure 10: Two-dimensional histogram of 94 GHz effective radar reflectivity computed, using the
727 Hammonds/Matrossov approach, from the 2D-S alone versus that computed from the 2D-S combined with the PIP.

728

729 Figure 11: Distributions of quantities computed using the parametric modified gamma distribution along with the
730 true values of N_0^* and D_m computed from the 2D-S alone and from the 2D-S combined with the PIP. (a) N_T (b)
731 extinction coefficient (c) IWC (d) 94 GHz effective radar reflectivity

732

733 Figure 12: Marginal pdfs of quantities computed directly from 2D-S data, as well as computed using the
734 parameterized 2D-S and the parameterized, uncorrected 2DC. (a) total number concentration (b) shortwave
735 extinction coefficient (c) ice water content (d) radar reflectivity

736

737 Figure 13: Marginal pdfs of quantities computed directly from 2D-S data, as well as computed using the
738 parameterized 2D-S and the parameterized, corrected 2DC. (a) total number concentration (b) shortwave extinction

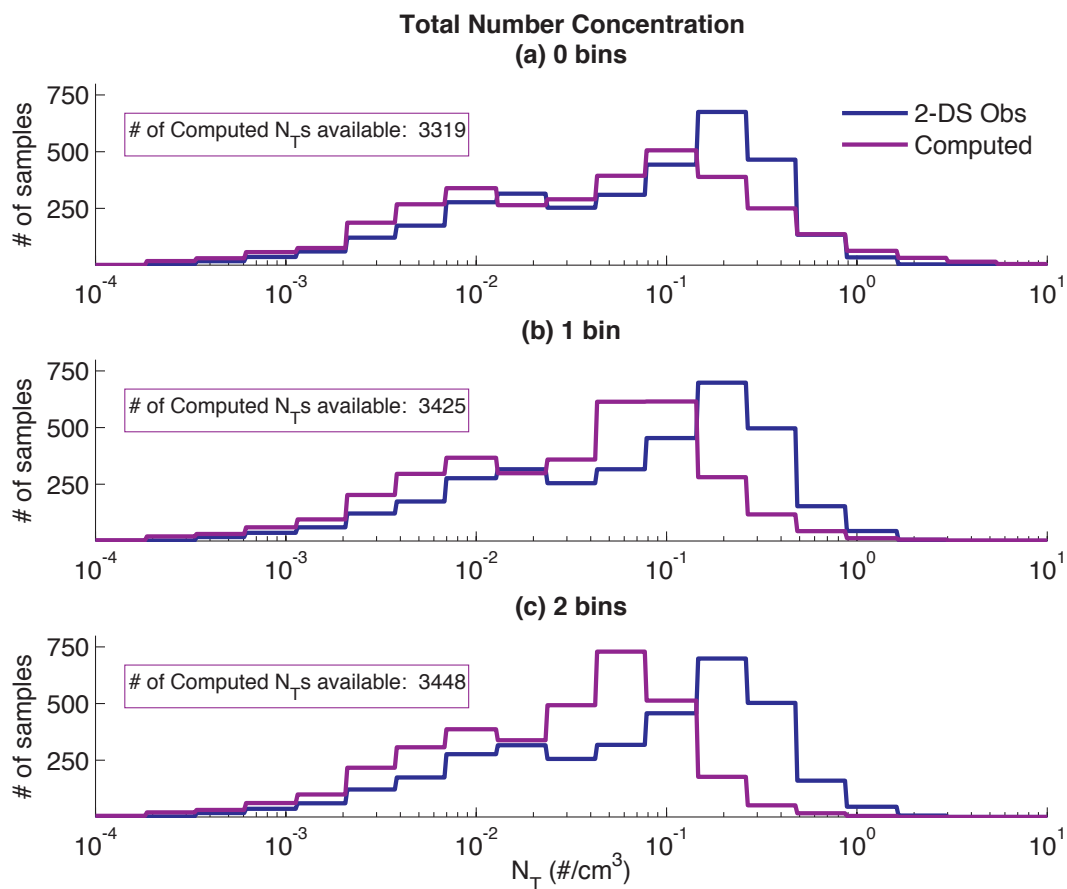
739

740

741



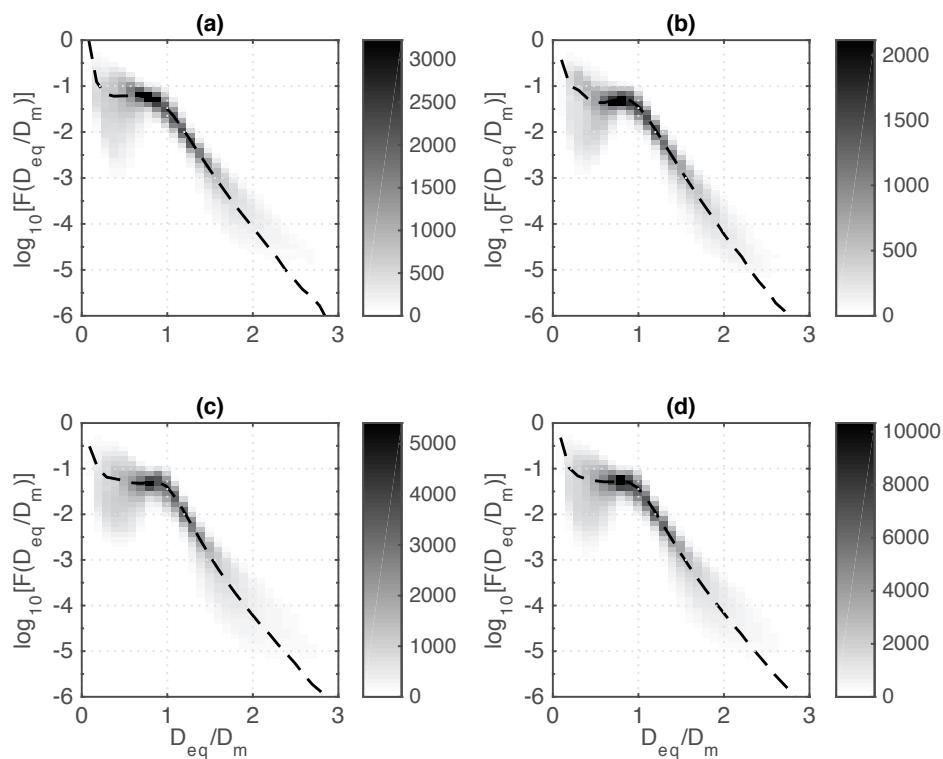
742 FIGURES
743
744



745
746
747

Figure 1: Comparisons of computed and measured total number concentration for 15-second PSD averages and for truncation of none through the first two PSD size bins.

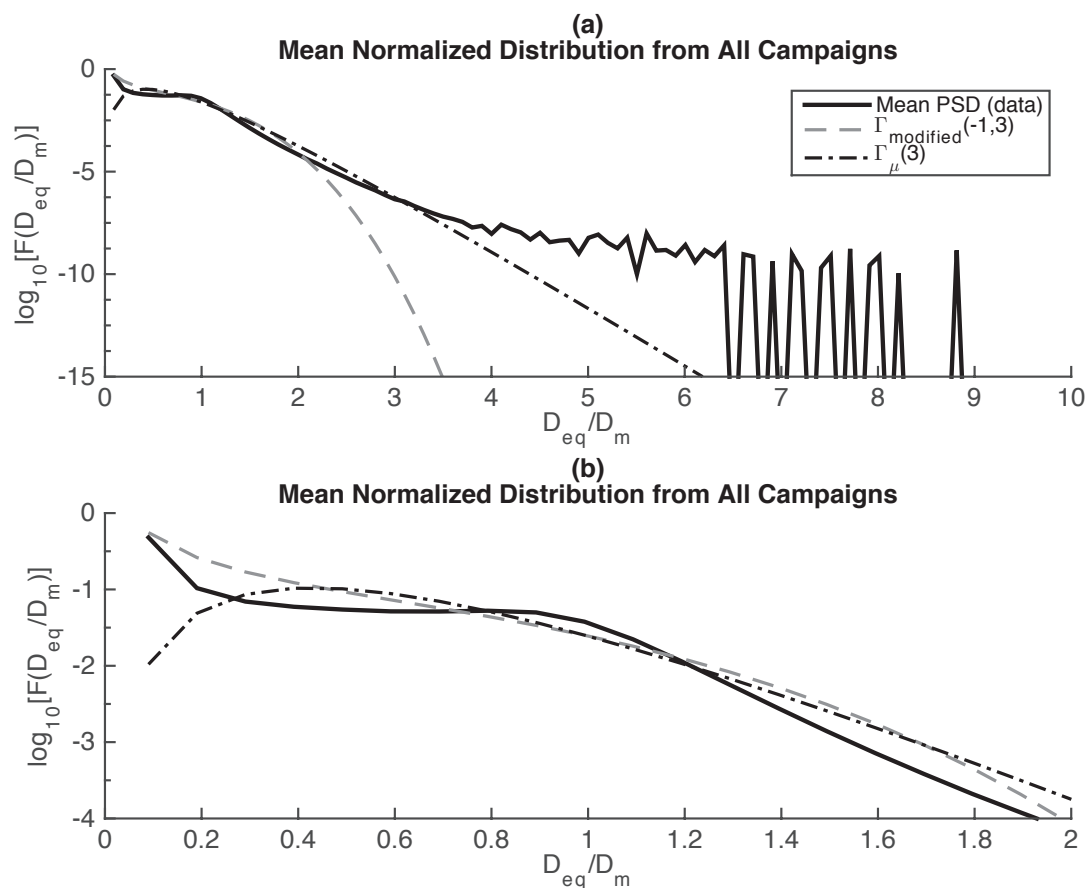
748
749



750
751
752
753

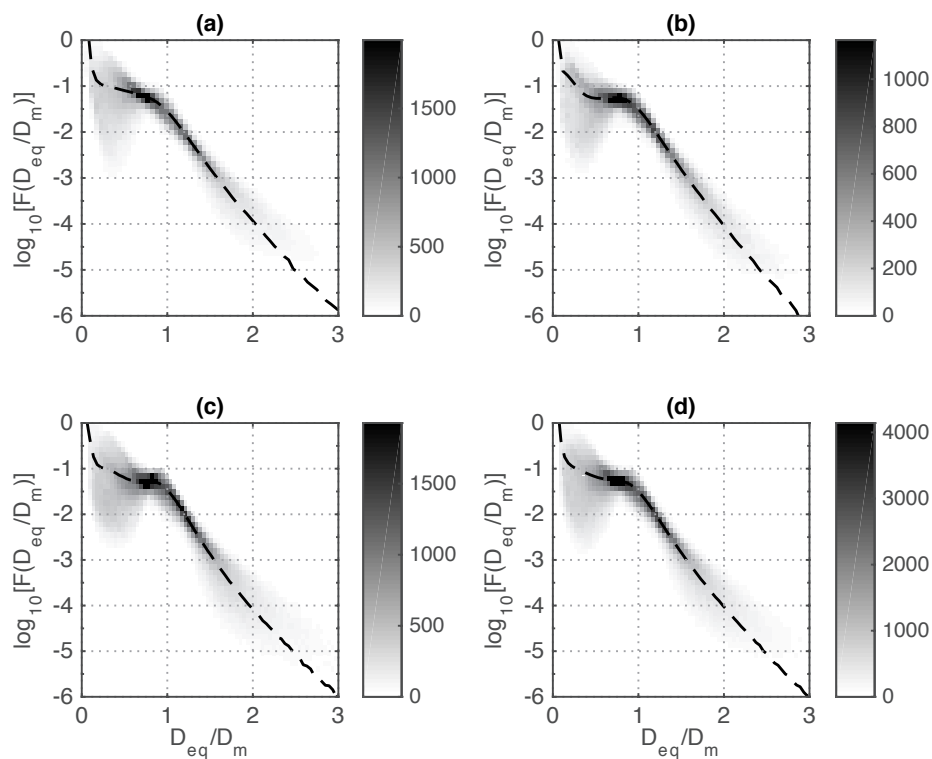
Figure 2: Histograms of normalized PSDs from each flight campaign, overlaid with their mean, normalized PSDs (D05 normalization). The color map is truncated at 75% of the highest number of samples in a bin so as to increase contrast. (a) TC⁴ (b) MACPEX (c) SPARTICUS (d) all data combined

754



755
 756
 757
 758
 759

Figure 3: The mean, normalized PSD (D05 normalization) from all three datasets combined, overlaid with two parameterizations from D05: the gamma-mu parameterization (dash-dotted curve) and the modified gamma parameterization (dashed curve). Panel (b) is a zoom-in on a portion of panel (a).



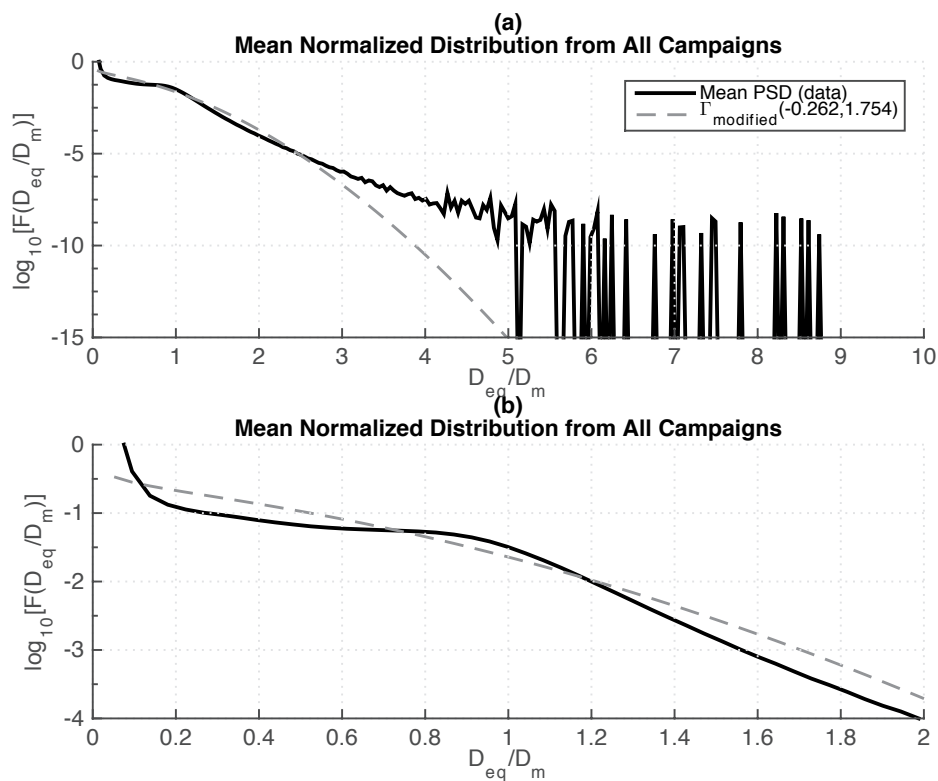
760
761

Figure 4: Same as Figure 2, but using D14 normalization.

762
763
764



765



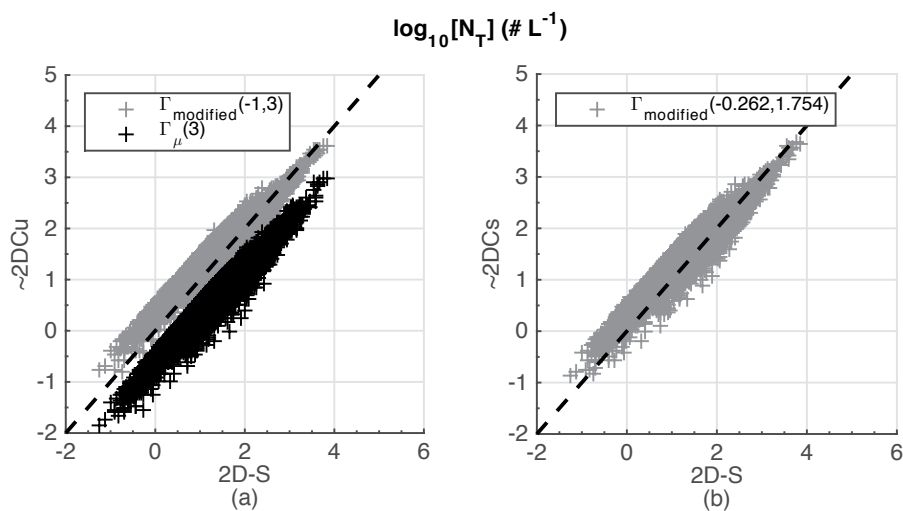
766
767
768

Figure 5: The mean, normalized PSD (D14 normalization) from all three datasets combined, overlaid with the parameterizations from D14. Panel (b) is a zoom-in on a portion of panel (a).

769
770



771



772

773

774

775

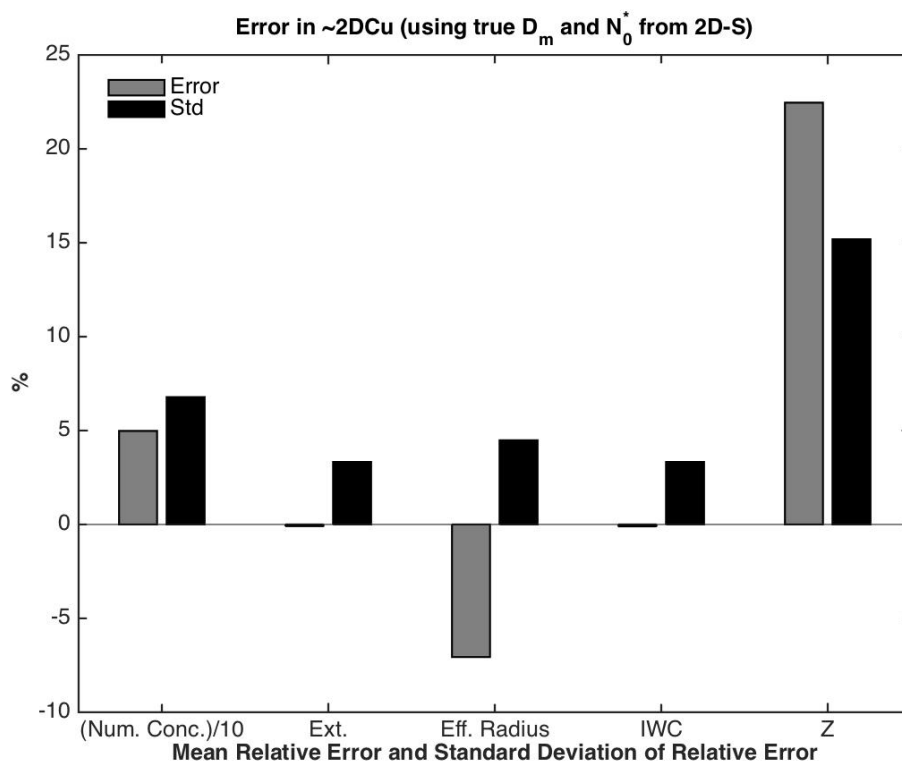
776

777

Figure 6: Total number concentration computed using the parameterized universal PSDs from D05 along with true values of N_0^* and D_m (from the 2D-S data) scattered vs. total number concentration computed directly from untransformed 2D-S data.



778



779

780

781

782

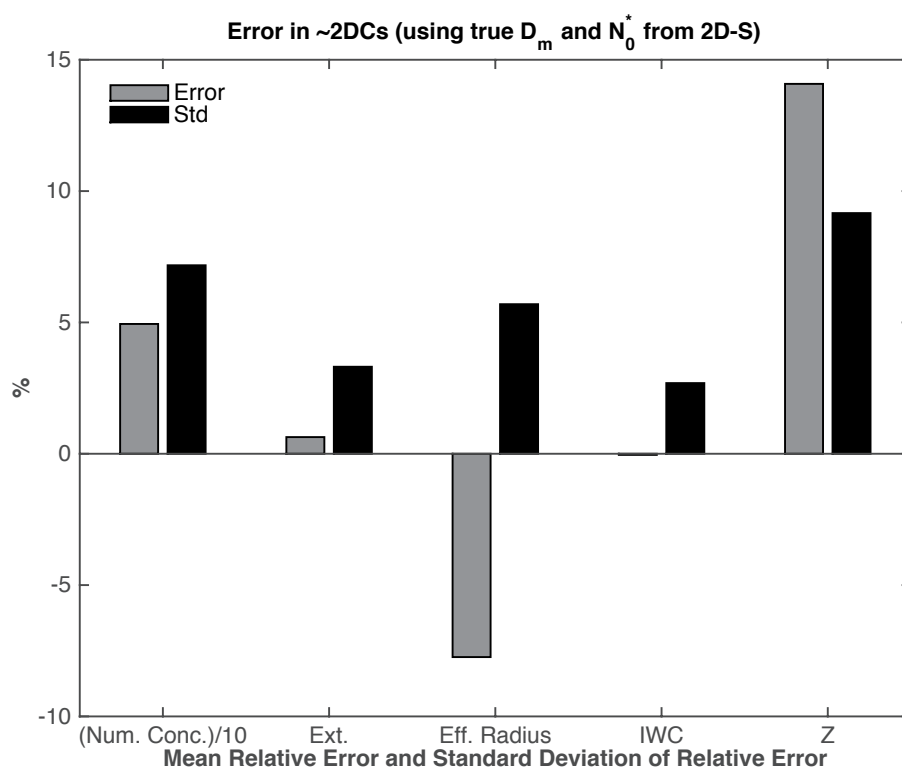
783

784

Figure 7: Mean relative error and standard deviation of the relative error between total number concentration (divided by 10), effective radius, IWC, and Z as computed directly from the 2D-S and as computed from the modified-gamma universal PSD shape and the true N_0^* and D_m computed from the 2D-S data.



785



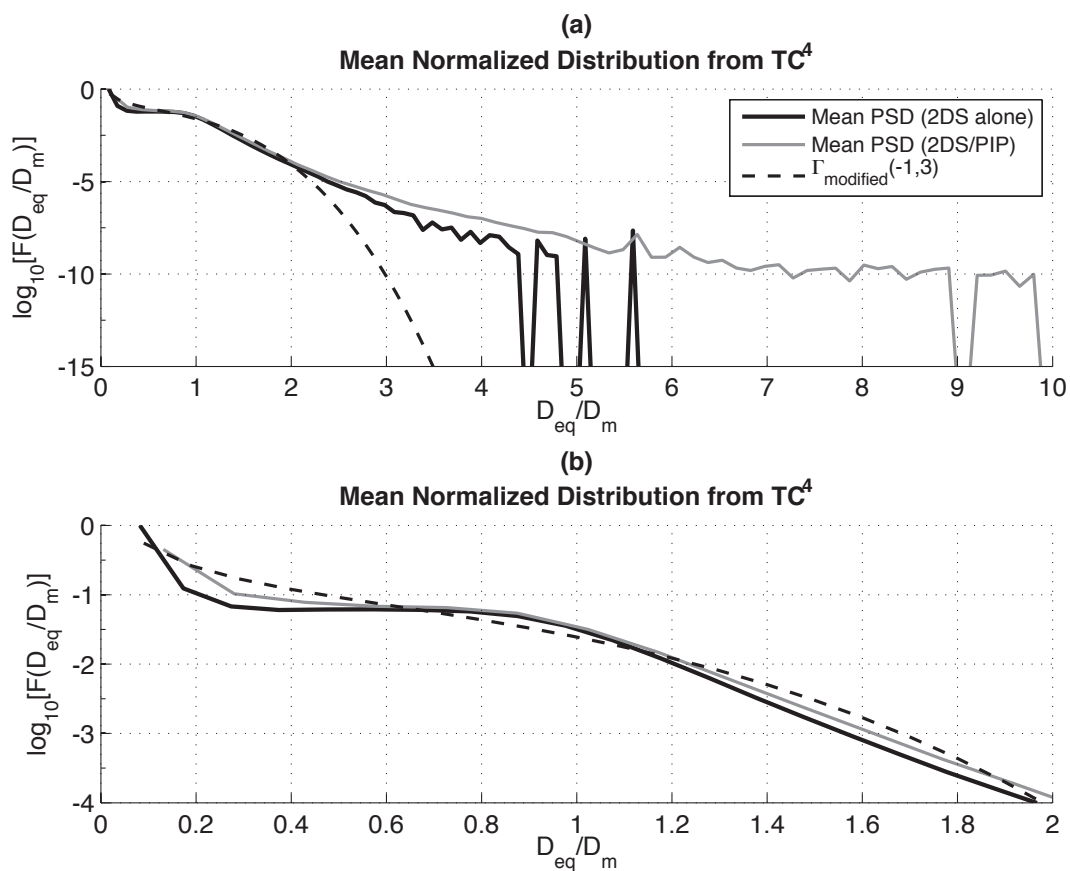
786
787

Figure 8: As in Figure 7, but using the shatter-corrected 2DC parameterization.

788
789



790
 791



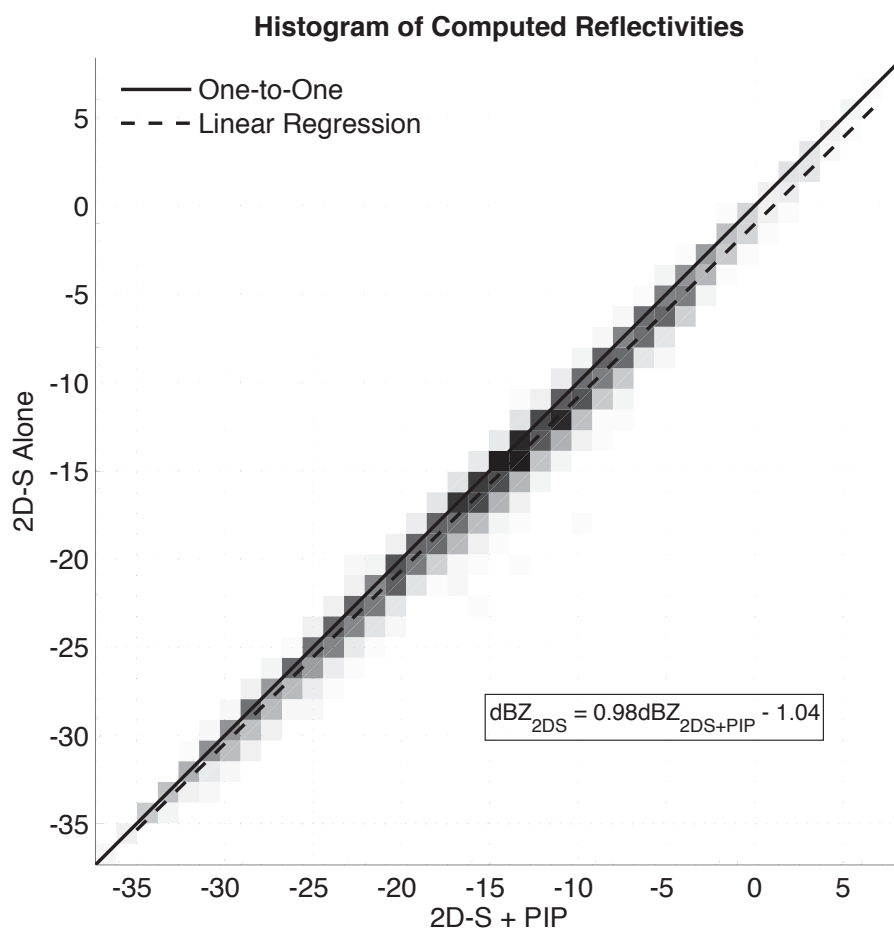
792
 793
 794
 795

Figure 9: Data from TC⁴ alone. The mean, normalized PSD from the 2D-S is overlaid with the mean, normalized PSD obtained from combining the 2D-S with the PIP and the modified gamma parameterization from D05 (dashed curve). Panel (b) is a zoom-in on a portion of panel (a).

796



797



798

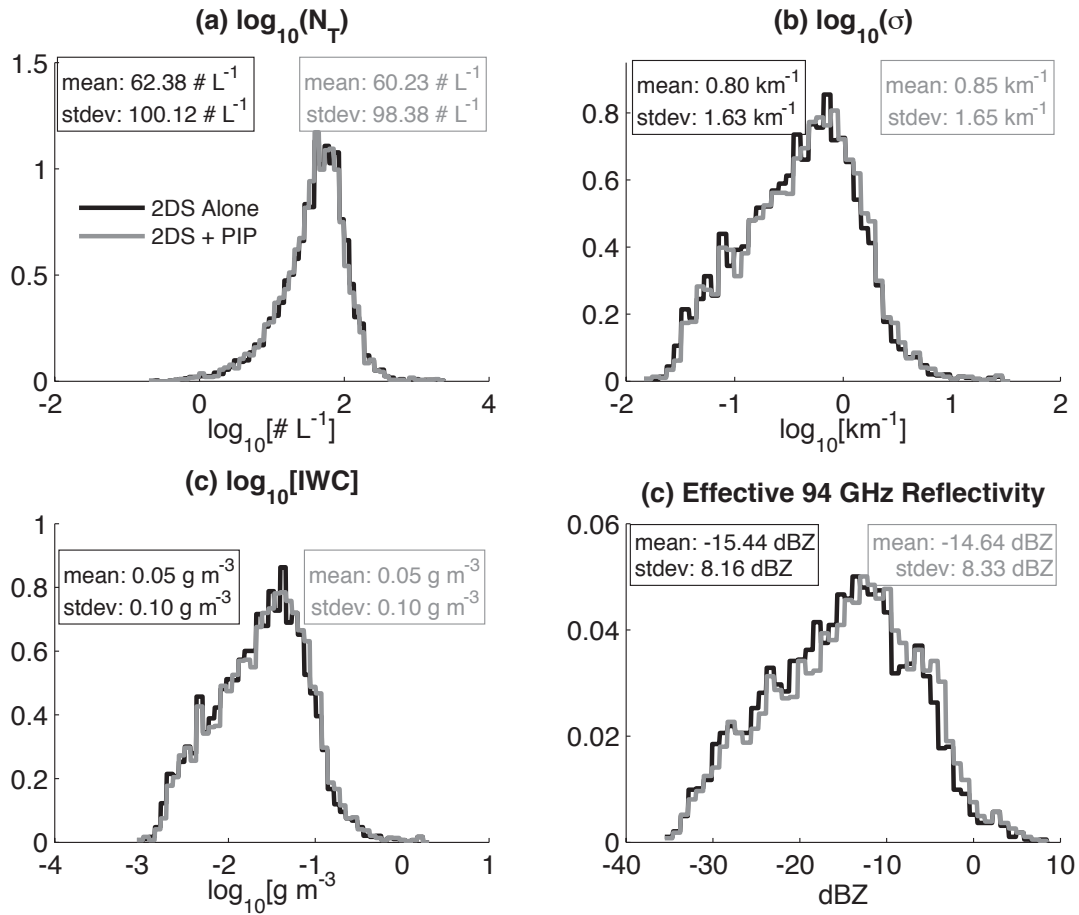
799

800

801

802

Figure 10: Two-dimensional histogram of 94 GHz effective radar reflectivity computed, using the Hammonds/Matrosov approach, from the 2D-S alone versus that computed from the 2D-S combined with the PIP.



803

804

805

806

807

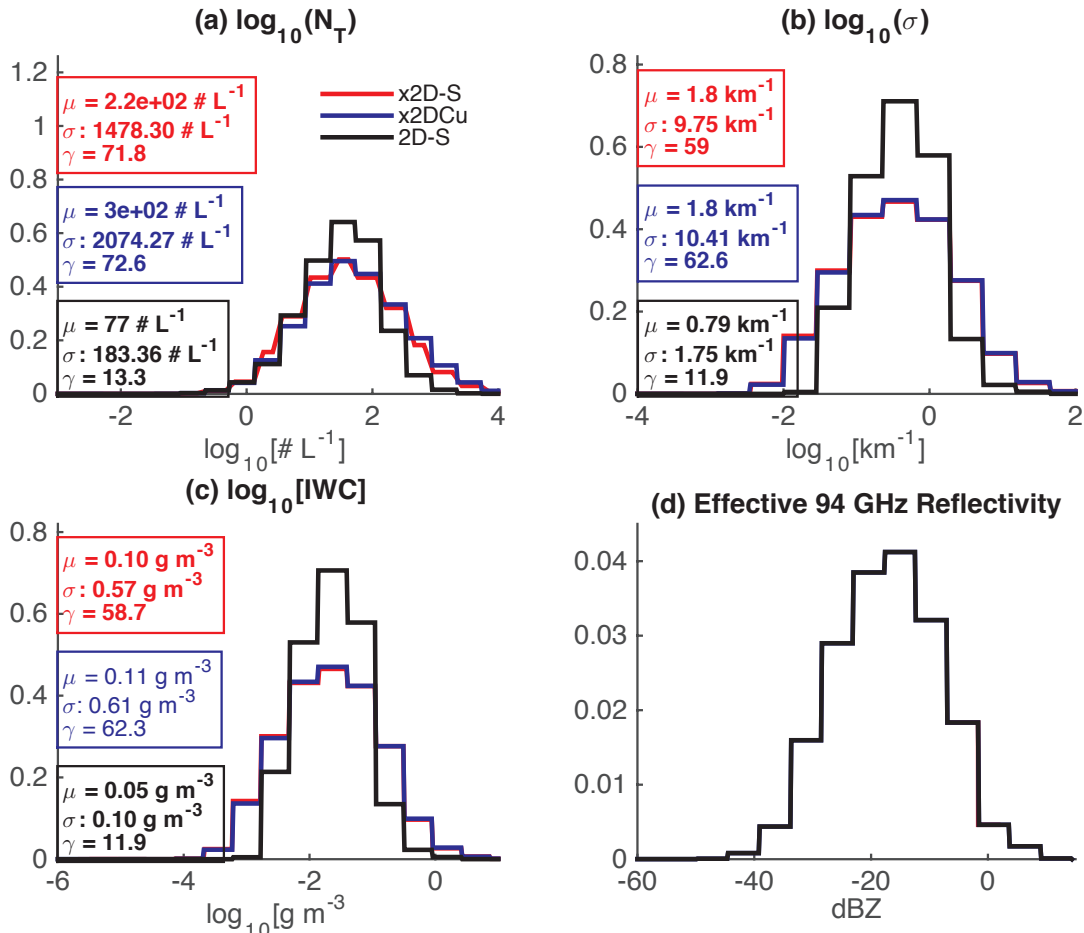
808

809

Figure 11: Distributions of quantities computed using the parametric modified gamma distribution along with the true values of N_0^* and D_m computed from the 2D-S alone and from the 2D-S combined with the PIP. (a) N_T (b) extinction coefficient (c) IWC (d) 94 GHz effective radar reflectivity



810



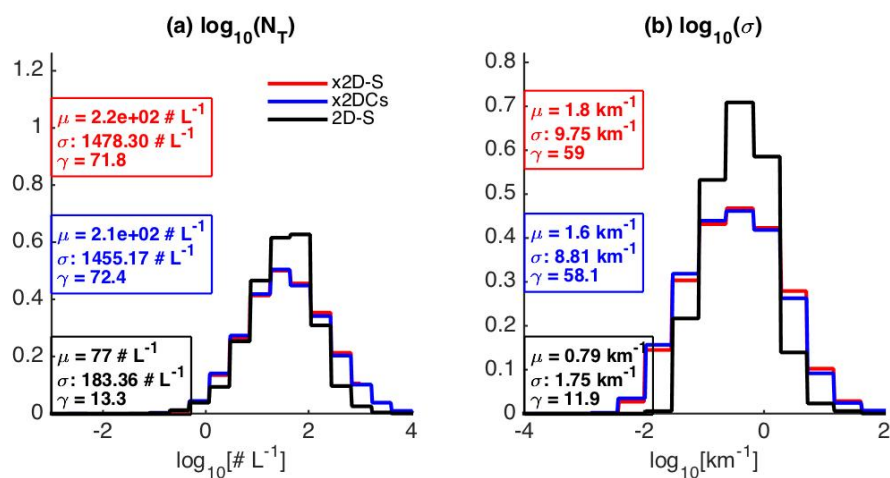
811
 812
 813
 814

Figure 12: Marginal pdfs of quantities computed directly from 2D-S data, as well as computed using the parameterized 2D-S and the parameterized 2DC. (a) total number concentration (b) shortwave extinction coefficient (c) ice water content (d) radar reflectivity

815



816



817
 818
 819
 820

Figure 13: Marginal pdfs of quantities computed directly from 2D-S data, as well as computed using the parameterized 2D-S and the parameterized, corrected 2DC. (a) total number concentration (b) shortwave extinction